Journal of Thermal Analysis and Calorimetry (2020) 140:1277–1291
https://doi.org/10.1007/s10973-019-09097-5

Enhancement of heat transfer in peristaltic flow in a permeable channel under induced magnetic field using different CNTs

M. Raza[1] · R. Ellahi[2,3] · Sadiq M. Sait[4] · M. M. Sarafraz[5] · M. S. Shadloo[6] · Ifraheem Waheed[2]

Received: 9 October 2019 / Accepted: 23 November 2019 / Published online: 21 December 2019

Abstract

The flow of salt water as a base fluid containing nanoparticles of different shapes, viz. zigzag, chiral, and armchair, in an asymmetric permeable channel has been investigated. Such particles in peristaltic flow with a magnetic field have noteworthy medical applications. Two illustrative models, namely those of Hamilton and Crosser, are utilized. The set of governing partial differential equations is solved analytically to find exact solutions, and numerical results are obtained using computer software. A rich summary of the latest findings for pertinent parameters and trapping phenomena is presented using graphs, tables, and streamline diagrams.

Keywords Nanoparticles · Peristaltic flow · MHD · Hamilton and Crosser models · Permeable channel · Analytical results · Numerical results

Introduction

A peristaltic pump is a type of positive displacement pump with two cavities, one for suction and the other for discharge, especially used for many types of liquid. During the operation of such a pump, fluid flows into the suction cavity and out of the discharge cavity as it collapses, the main constraint being that the volume of fluid remains constant in any given cycle. The whole process is known as peristalsis and can be observed extensively in biological systems such as the gastrointestinal tract, as well as in heart–lung machines, which are used to maintain normal blood circulation during bypass surgery or kidney dialysis. In fluid mechanics literature, pioneering work on peristalsis in relation to mechanical pumping was carried out by Latham [1], after which Shapiro et al. [2] were the first to study peristaltic transport of Newtonian fluids in the wave frame of reference, while Fung and Yih [3] again studied peristalsis but in the laboratory frame. At the start of the 20th century, Mishra and Ramachandra [4] reported on peristaltic flow in channels with asymmetry generated by peristaltic waves of different amplitudes, concluding that, in comparison with a symmetric channel, a thinner reflux layer, lower trapping zone, and lower flux were obtained. Meanwhile, peristaltic flow of different phases has also been discussed [5–7].

In the current technological era, a main area of focus has been improving heat transfer and decreasing the thermal conductivity of fluids such as water, oil, and ethylene–glycol mixtures. It is well known that the conductivity of some solids is always higher than that of liquids, thus the main effect of addition of particles into such fluids is to enhance their heat transfer features. However, such addition of particles of different sizes faces two main hurdles:

(a) The increased pressure drop in the system.
(b) The inhomogeneity of the mixed system.

✉ R. Ellahi
rellahi@alumni.ucr.edu; rahmatellahi@yahoo.com

1 Department of Mathematics, Northern University Nowshera, KPK, Nowshera 54000, Pakistan

2 Department of Mathematics and Statistics, IIUI, H-10, Islamabad, Pakistan

3 Center for Modeling and Computer Simulation, Research Institute, KFUPM, Dhahran, Saudi Arabia

4 Center for Communications and IT Research, Research Institute, King Fahd University of Petroleum and Minerals, Dhahran 31261, Saudi Arabia

5 School of Mechanical Engineering, The University of Adelaide, Adelaide, SA, Australia

6 CORIA-CNRS (UMR6614), Normandie University, INSA of Rouen, 76000 Rouen, France

As a result, scientists have focused on addition of nanoparticles, whose similar size to that of the fluid molecules in the base fluids offers two main advantages:

(i) The particles can move along with the molecules in the fluid; i.e., they act like the fluid;
(ii) They remain stable for long times because of the very low differential effect of gravity.

Such a combination of nanosized particles suspended in a conductive base fluid is known as a nanofluid, as explained in detail by Buongiorno [8], who showed that the relative velocity can be easily expressed as the sum of the velocity of the base fluid and its relative slip velocity, leading to the requirement for a realistic model for these two components of the effects in nanofluids. The findings of that work include that:

- In a nanofluid, two very important factors are Brownian diffusion and thermophoresis of the nanoparticles, and the slip effect of the base liquid;
- A two-part inhomogeneous equilibrium model can be developed to described the Brownian diffusion and thermophoresis;
- The energy transfer by nanoparticles can be considered to be negligible (although other literature disagrees in this regard);
- Results for the correlation structure can be obtained, in good agreement with other literature.

The nanoparticles suspended in the base fluid are usually made of metals, oxides, carbides, or carbon nanotubes, while the base fluid mat be water or ethylene glycol, as used by different authors, or some type of oil. The first use of the term "nanofluid" was by Choi [9], a pioneering researcher on this topic. Choi concluded that nanofluids represent a unique type of material and proposed that high-thermal-conductivity nanofluids could be analyzed with the help of the HM (Hamilton and Crosser) model for the studied copper–water nanofluid. This was also verified experimentally by Masuda [10] for another type of particles, viz. Al_2O_3. That author also explained some very prominent benefits of nanofluids with copper nanophase and explained them analytically, including the unexpected reduction in the pumping power required for a heat exchanger when using a nanofluid; For example, if heat source power of 10 W m^{-2} K^{-1} achieves heat transfer of 2 W m^{-2} K^{-1}, the same can be achieved with a reduced heat source power of 3 W m^{-2} K^{-1} when using a nanofluid.

Carbon nanotubes (CNTs) are another important type of nanoparticles; they are another form of carbon, being similar to graphite, which is seen extensively in daily life, e.g., in lead pencils. CNTs are hollow cylindrical tubes with size 10,000 times smaller than a human hair but stronger than steel. They are also highly electrically conductive, which could make them an extremely cost-effective replacement for metal wires. The semiconducting properties of CNTs make them candidates for use in next-generation computer chips. Nanotubes were discovered by Iijima [11] and Baughman et al. [12]. There are two main types of nanotubes, viz. single-walled nanotubes (SWNTs) and multiwalled nanotubes (MWNTs). A single-walled carbon nanotube is just like a regular straw, having only one layer or wall. Multiwalled carbon nanotubes are formed from a collection of nested tubes of increasing diameter. Carbon nanotubes exhibit extraordinary thermal conductivity, electrical conductivity, and mechanical properties, finding applications as additives for structural materials used in golf clubs, boats, aircraft, bicycles, etc. Mixing CNTs into solids [13–16] or fluids [17–23] can effectively enhance the thermal and mechanical properties of the base material, leading to wide study of their use in heat transfer applications [24–27].

Magnetohydrodynamics (MHD) is the study of the magnetic properties of electrically conducting fluids. Examples of such magnetofluids include plasmas, liquid metals, and salt water or electrolytes [28–38].

Despite the studies cited above, peristaltic flow containing CNT nanoparticles in an induced magnetic field in a permeable channel has not been studied using the Crosser model; The objective of this paper is to fill this gap in the literature.

Mathematical formulation

Consider the flow of a nanofluid containing SWCNTs with zigzag, chiral, and armchair shape in salt water as base fluid in a channel with a permeable wall having width $d_1 + d_2$. An external uniform constant transverse magnetic field H_0 is applied, inducing a magnetic field $H\left(h_X(X,Y,t), H_0 + h_Y(X,Y,t), 0\right)$ and a total magnetic field $H^+\left(h_X(X,Y,t), H_0 + h_Y(X,Y,t), 0\right)$. The undulations in the channel profile [39–41] lead to

$$
\begin{aligned}
Y &= \bar{H}_1 = d_1 + a_1 \cos\left(\frac{2\pi}{\lambda}\left(\bar{X} - c_1\bar{t}\right)\right), \\
Y &= \bar{H}_2 = -d_2 - b_1 \cos\left(\frac{2\pi}{\lambda}\left(\bar{X} - c_1\bar{t}\right) + \omega\right).
\end{aligned} \tag{1}
$$

In Eq. (1), a_1 and b_1 are wave amplitudes, λ is the wavelength, ω is the amplitude ratio, $d_1 + d_2$ is the channel width, c_1 is the wave speed, $\bar{t}$ is time, $\bar{X}$ is the direction of wave propagation while Y is perpendicular to as shown in Fig. 1.

A mathematical model in the general form can be expressed as follows:

$$
\nabla \cdot \mathbf{H} = 0, \nabla \cdot \mathbf{E} = 0, \tag{2}
$$

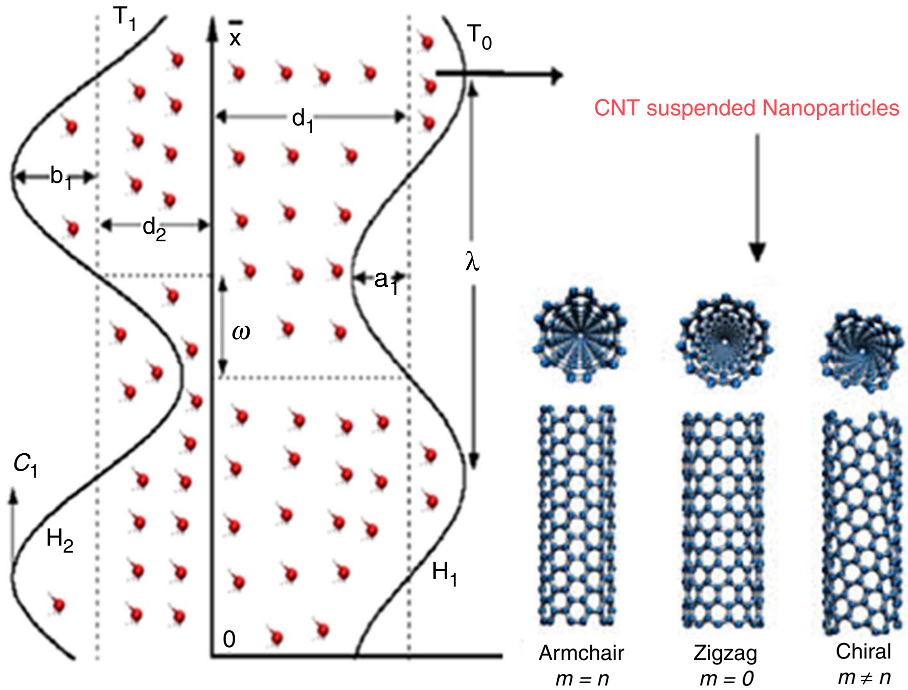

Fig. 1 Flow diagram

$$\nabla \wedge \mathbf{H} = \mathbf{J}, \quad \mathbf{J} = \sigma\left\{\mathbf{E} + \mu_e(\mathbf{V} \wedge \mathbf{H})\right\}, \tag{3}$$

$$\nabla \wedge \mathbf{E} = -\mu_e \frac{\partial \mathbf{H}}{\partial \mathbf{t}}. \tag{4}$$

The continuity equation can be written as

$$\nabla.\mathbf{V} = 0. \tag{5}$$

The equations of motion are

$$\rho_{nf}\left(\frac{\partial \boldsymbol{V}}{\partial t} + \boldsymbol{V}\cdot\nabla\boldsymbol{V}\right) = -\nabla p + \mu_{nf}\nabla^2\boldsymbol{V} + (\rho\beta)_{nf} g\alpha\left(T - T_0\right) - \nabla\left(\frac{1}{2}\mu_e\left(\boldsymbol{H}^+\right)^2\right) - \mu_e\left(\boldsymbol{H}^+\cdot\nabla\right)\boldsymbol{H}. \tag{6}$$

The energy equation can be expressed as

$$(\rho c)_{nf}\left(\frac{\partial \mathbf{T}}{\partial t} + \mathbf{V}\cdot\nabla\mathbf{T}\right) = k_{nf}\nabla^2 T + Q_0 - \frac{\partial q}{\partial y}, \tag{7}$$

where

$$q = \frac{4\sigma^*}{3k^*}\frac{\partial T^4}{\partial y}. \tag{8}$$

Expanding in a Taylor's series about T_∞ and ignoring higher-order terms yields

$$T^4 \approx 4T_\infty^3 T - 3T_\infty^4. \tag{9}$$

Combining Eqs. (2)–(4) provides

$$\frac{\partial \mathbf{H}^+}{\partial t} = \nabla \wedge \left(\mathbf{V} \wedge \mathbf{H}^+\right) + \frac{1}{\xi}\nabla^2\mathbf{H}^+. \tag{10}$$

Using the static wave structures

$$x = X - ct, y = Y, u = U - c, v = V, \tag{11}$$

and applying the transformations

$$\bar{p} = \frac{a^2}{\mu_f c\lambda}p,\ \bar{u} = \frac{\lambda}{ac}u,\ \bar{v} = \frac{v}{c},\ \bar{y} = \frac{y}{\lambda},\ \bar{x} = \frac{x}{a},\ \bar{t} = \frac{c}{\lambda}t,\ D_a = \frac{k}{a^2},$$
$$\mathrm{Re} = \frac{\rho c a}{\mu_f},\ \delta = \frac{a}{\lambda},\ \bar{\theta} = \frac{T - T_0}{T_0},\ \bar{\Phi} = \frac{\Phi}{H_0 a},\ \bar{\Psi} = \frac{\Psi}{ca},\ R_m = \sigma\mu_e ac,$$
$$\overline{h_x} = \bar{\Phi}_{\bar{x}},\ \overline{h_y} = -\bar{\Phi}_{\bar{y}},\ G_r = \frac{\rho_f g\alpha a^2}{\mu_f c}(T_0),\ S_1 = \frac{H_0}{c}\sqrt{\frac{\mu_e}{\rho}},$$
$$\alpha_{nf} = \frac{k}{(\rho c)_f},\ \tau = \frac{(\rho c)_p}{(\rho c)_f}. \tag{12}$$

in Eq. (11) and taking $\delta \to 0$, the following dimensionless system of equations without bars is obtained:

$$\frac{\partial u}{\partial x} + \frac{\partial v}{\partial y} = 0, \tag{13}$$

$$\frac{dp}{dx} = \frac{\partial^3\Psi}{\partial y^3}\left(\frac{\mu_{nf}}{\mu_f}\right) + \mathrm{Re}S_1^2\Phi_{yy} + \frac{(\rho\beta)_{nf}}{(\rho\beta)_f}\frac{G_r}{\mathrm{Re}}\theta, \tag{14}$$

$$\frac{dp}{dy} = 0, \tag{15}$$

$$\Phi_{yy} = R_m\left(E - \frac{\partial \Psi}{\partial y}\right), \tag{16}$$

$$\left(\frac{k_{nf}}{k_f} - N\right)\frac{\partial^2\theta}{\partial y^2} + Q_0\theta = 0. \tag{17}$$

Applying Eq. (16) in Eq. (14) yields

$$\frac{dp}{dx} = \frac{\partial^3\Psi}{\partial y^3}\left(\frac{\mu_{nf}}{\mu_f}\right) + \mathrm{Re}S_1^2R_m\left(E - \frac{\partial\Psi}{\partial y}\right) + \frac{(\rho\beta)_{nf}}{(\rho\beta)_f}G_r\theta. \tag{18}$$

Differentiating Eq. (18) with respect to y yields

$$\frac{\partial^4\Psi}{\partial y^4}\left(\frac{\mu_{nf}}{\mu_f}\right) + \mathrm{Re}S_1^2R_m\left(-\frac{\partial^2\Psi}{\partial y^2}\right) + \frac{(\rho\beta)_{nf}}{(\rho\beta)_f}\frac{G_r}{\mathrm{Re}}\frac{\partial\theta}{\partial y} = 0. \tag{19}$$

The nondimensional boundary conditions can be expressed as

$$\Psi = \frac{F}{2}, \frac{\partial\Psi}{\partial y} = -1 - \frac{\sqrt{D_a}}{\alpha}\frac{\partial^2\Psi}{\partial y^2} \quad \text{at } y = h_1, \tag{20}$$

$$\Psi = -\frac{F}{2}, \frac{\partial\Psi}{\partial y} = -1 + \frac{\sqrt{D_a}}{\alpha}\frac{\partial^2\Psi}{\partial y^2} \quad \text{at } y = h_2, \tag{21}$$

$$\theta = 0 \quad \text{at } y = h_1, \ \theta = 1 \quad \text{at } y = h_2, \tag{22}$$

$$\Phi = 0 \quad \text{at } y = h_1, \quad \Phi = 0 \text{ at } y = h_2. \tag{23}$$

The pressure rise Δp, magnetic factor h_x, and current density J_z can be expressed nondimensionally as

$$\Delta p = \int_0^1 \left(\frac{dp}{dx}\right)dx, \tag{24}$$

$$h_x = \frac{\partial\Phi}{\partial y}, \tag{25}$$

$$J_z = -\frac{\partial h_x}{\partial y}. \tag{26}$$

Meanwhile, the thermophysical relations are

$$\rho_{nf} = (1-\phi)\rho_f + \phi\rho_s, \tag{27}$$

$$(\rho C_p)_{nf} = (1-\phi)(\rho C_p)_f + \phi(\rho C_p)_s, \tag{28}$$

$$\beta_{nf} = \frac{(1-\phi)(\rho\beta)_f + \phi(\rho\beta)_s}{\rho_{nf}}, \tag{29}$$

$$\alpha_{nf} = \frac{k_{nf}}{(\rho C_p)_{nf}}. \tag{30}$$

Based on existing literature [42], one can write

$$\frac{\mu_{nf}}{\mu_f} = (1 - A_1\phi), \tag{31}$$

where A_1 is defined as

$$A_1 = \frac{0.312\gamma^* - 0.5}{\ln 2\gamma^* - 1.5} + 2 - \frac{1.872}{\gamma^*}, \tag{32}$$

with

$$\gamma^* = \frac{\sqrt{\tilde{a}^2 + \tilde{b}^2 + \tilde{c}^2}}{\tilde{a}\tilde{b}\tilde{c}}, \tag{33}$$

$$\tilde{b} = \tilde{c} = \tilde{d}/2, \tag{34}$$

$$\tilde{a} \gg \tilde{b} = \tilde{c}, \tag{35}$$

in which $\tilde{d}$ is the diameter of the CNT particles of different shapes, given by

$$\tilde{d} = \frac{a^*}{\pi}\sqrt{n^{*2} + n^*m^* + m^{*2}}, \tag{36}$$

where $a^* = 0.246$ nm.

The Hamilton and Crosser models [43] are chosen, expressed as follows:

$$\frac{k_{nf}}{k_f} = \frac{K_s + (n^{**}-1)K_f - (n^{**}-1)(K_f - K_s)\phi}{K_s + (n^{**}-1)K_f + \phi(K_f - K_s)}, \tag{37}$$

$$n^{**} = \frac{3}{\alpha}, \tag{38}$$

$$\psi = \frac{\pi^{1/3}(6V_p)^{2/3}}{A_p}, \tag{39}$$

where $V_p = \pi r^2 h$ is the volume and $A_p = 2\pi r(r+h)$ is the surface area of a particle and $r = \tilde{b} = \tilde{c}$, $h = \tilde{a}$. The thermophysical properties are presented in Table 1.

Table 1 Thermophysical properties

Physical property	Salt water	SWCNT	MWCNT
ρ/kg m^{-3}	1112	2600	1600
C_p		425	796
$\beta\times10^5$/K^{-1}	18.5	2.6	2.8
k/W m^{-1} K^{-1}	0.51	6600	3000

Analytical results

Using routine manipulations, these analytical results can be expressed as follows:

$$\theta = \operatorname{csch}\left(\frac{(h_1 - h_2)\sqrt{Q_0}}{\sqrt{-\frac{k_{\mathrm{nf}}}{k_{\mathrm{f}}} + N}}\right)\sinh\left(\frac{\sqrt{Q_0}(h_1 - y)}{\sqrt{-\frac{k_{\mathrm{nf}}}{k_{\mathrm{f}}} + N}}\right), \tag{40}$$

$$\Psi = C_3 + C_4 y + \frac{1}{\mathrm{Re}}\left(\begin{array}{l} \frac{M_1 C_2 \mathrm{e}^{-\mathrm{M}_{11}}}{R_{\mathrm{m}} S_1^2} + \frac{M_1 C_1 \mathrm{e}^{\mathrm{M}_{11} y}}{R_{\mathrm{m}} S_1^2} - \\ \frac{M_2 G_{\mathrm{r}} (M_9)^{3/2} \operatorname{Cosh}(M_6) \operatorname{Cosh}(M_5) \operatorname{Csch}(M_7)}{M_{13}} \\ + \frac{M_2 G_{\mathrm{r}} (M_9)^{3/2} \operatorname{Csch}(M_7) \operatorname{Sinh}(M_6) \operatorname{Sinh}(M_5)}{M_{13}} \end{array}\right), \tag{41}$$

$$\Phi = \left.\begin{array}{l} \frac{M_1^{3/2} \mathrm{e}^{\mathrm{M}_{11} y}\left(-C_1 + C_2 \mathrm{e}^{-2\mathrm{M}_{11} y}\right)}{\mathrm{Re}^{3/2}\sqrt{R_{\mathrm{m}}} S_1^3} - \frac{1}{2} C_4 R_{\mathrm{m}} y^2 + \frac{1}{2} E R_{\mathrm{m}} y^2 + C_5 + y C_6 - \\ \frac{M_2 G_{\mathrm{r}} M_9^{3/2} R_{\mathrm{m}} \operatorname{Cosh}(M_5) \operatorname{Csch}(M_7) \operatorname{Sinh}(M_6)}{\mathrm{Re} M_{13}} + \\ \frac{M_2 G_{\mathrm{r}} M_9^{3/2} R_{\mathrm{m}} \operatorname{Cosh}(M_6) \operatorname{Csch}(M_7) \operatorname{Sinh}(M_5)}{\mathrm{Re} M_{13}} \end{array}\right\}, \tag{42}$$

The mean volume flow rate Q is

$$Q = 1 + F. \tag{43}$$

The pressure gradient $\mathrm{d}p/\mathrm{d}x$, axial induced magnetic field h_{x}, and current density j_{z} are given as

$$\frac{\mathrm{d}p}{\mathrm{d}x} = -\left.\frac{\left(\begin{array}{l} 2\operatorname{Csch}(M_7)\sinh\left(\frac{M_7}{2}\right) \\ \left(\begin{array}{l} G_{\mathrm{r}} M_2 (N - M_3)\left(\begin{array}{l} \sqrt{D_\alpha}\left(\mathrm{e}^{\mathrm{h}_1 \mathrm{M}_{11}} - \mathrm{e}^{\mathrm{h}_2 \mathrm{M}_{11}}\right) M_{10}\sinh\left(\frac{M_7}{2}\right)(N - M_3) + \\ \left(\mathrm{e}^{\mathrm{h}_1 \mathrm{M}_{11}} + \mathrm{e}^{\mathrm{h}_2 \mathrm{M}_{11}}\right)\sqrt{\mathrm{Re}}\sqrt{R_{\mathrm{m}}} S_1 \alpha \sinh\left(\frac{M_7}{2}\right)\sqrt{M_1}(N - M_3) \\ 2\left(\mathrm{e}^{\mathrm{h}_1 \mathrm{M}_{11}} - \mathrm{e}^{\mathrm{h}_2 \mathrm{M}_{11}}\right)\alpha M_1 \end{array}\right) \\ \sqrt{N1 - M_3}\sqrt{Q_0}(N M_{10} - M_{10} M_3 - M_1 Q_0) \end{array}\right) \end{array}\right)}{\left(\begin{array}{l} \mathrm{Re}\left(\begin{array}{l} \sqrt{D_\alpha}\left(\mathrm{e}^{\mathrm{h}_1 \mathrm{M}_{11}} - \mathrm{e}^{\mathrm{h}_2 \mathrm{M}_{11}}\right)(h_1 - h_2) M_{10} + \\ \left(\mathrm{e}^{\mathrm{h}_1 \mathrm{M}_{11}} + \mathrm{e}^{\mathrm{h}_2 \mathrm{M}_{11}}\right)(h_1 - h_2)\sqrt{\mathrm{Re}}\sqrt{R_{\mathrm{m}}} S_1 \alpha \sqrt{M_1} - 2\left(\mathrm{e}^{\mathrm{h}_1 \mathrm{M}_{11}} - \mathrm{e}^{\mathrm{h}_2 \mathrm{M}_{11}}\right)\alpha M_1 \end{array}\right) \\ \sqrt{N - M_3}\sqrt{Q_0}(N M_{10} - M_{10} M_3 - M_1 Q_0) \end{array}\right)}\right\}, \tag{44}$$

$$h_{\mathrm{x}} = \frac{1}{2}\left.\left(\begin{array}{l} C_4 R_{\mathrm{m}}(h_1 + h_2 - 2y) - E R_{\mathrm{m}}(h_1 + h_2 - 2y) - \frac{2 G_{\mathrm{r}} R_{\mathrm{m}} \cosh(M_8) \operatorname{Csch}(M_7) M_2 (N - M_3)^{3/2}}{\mathrm{Re}\sqrt{Q_0}(M_{10} M_9 + M_1 Q_0)} + \\ \frac{2\left(\begin{array}{l} -\frac{\mathrm{e}^{-\mathrm{M}_{11} y}\left(C_2 + C_1 \mathrm{e}^{2M_{11} y}\right)\sqrt{\mathrm{Re}} M_1}{S_1^2} + \frac{\mathrm{e}^{-(\mathrm{h}_1 + \mathrm{h}_2)\mathrm{M}_{11}}\left(\mathrm{e}^{\mathrm{h}_1 \mathrm{M}_{11}} - \mathrm{e}^{\mathrm{h}_2 | textM_{11}}\right)\left(C_2 + C_1 \mathrm{e}^{(\mathrm{h}_1 + \mathrm{h}_2)\mathrm{M}_{11}}\right) M_1^{3/2}}{(h_1 - h_2)\sqrt{R_m} S_1^3} \\ + \frac{G_r \sqrt{\mathrm{Re}} R_{\mathrm{m}} M_2 (N - M_3)^2}{(h_1 - h_2) Q_0 (M_{10}(-N + M_3) + M_1 Q_0)} \end{array}\right)}{\mathrm{Re}^{3/2}} \end{array}\right)\right\}, \tag{45}$$

$$j_{\mathrm{z}} = \left.\begin{array}{l} \frac{\mathrm{e}^{-\mathrm{M}_{11} y}\left(-C_2 + C_1 \mathrm{e}^{2\mathrm{M}_{11} y}\right)\sqrt{R_{\mathrm{m}}}\sqrt{M_1}}{\sqrt{\mathrm{Re}} S_1} + \\ \frac{R_{\mathrm{m}}\left(G_{\mathrm{r}} \operatorname{Csch}(M_7)\sinh(M_8) M_2 (N - M_3) + (C_4 - E)\mathrm{Re}(M_{10}(N - M_3) - M_1 Q_0)\right)}{\mathrm{Re}(M_{10}(N - M_3) - M_1 Q_0)} \end{array}\right\}, \tag{46}$$

where the constants M_1–M_{13} are given by

$$\begin{array}{l} M_1 = A = \frac{\mu_{\mathrm{nf}}}{\mu_{\mathrm{f}}}, M_2 = B = \frac{(\rho\beta)_{\mathrm{nf}}}{(\rho\beta)_{\mathrm{f}}}, M_3 = Kf = \frac{k_{\mathrm{nf}}}{k_{\mathrm{f}}}, \\ M_4 = \frac{\sqrt{Q_0}}{\sqrt{-Kf + N}} M_5 = \frac{\sqrt{Q_0} y}{\sqrt{-Kf + N}}, M_6 = \frac{h_1\sqrt{Q_0}}{\sqrt{-Kf + N}}, \\ M_7 = \frac{(h_1 - h_2)\sqrt{Q_0}}{\sqrt{-Kf + N}}, M_8 = \frac{\sqrt{Q_0}(h_1 - y)}{\sqrt{-Kf + N}} \\ M_9 = Kf - N, M_{10} = \mathrm{Re} R_{\mathrm{m}} S_1^2, M_{11} = \frac{\sqrt{\mathrm{Re}}\sqrt{R_{\mathrm{m}}} S_1}{\sqrt{A}}, M_{12} = R_{\mathrm{m}} S_1^2 \\ M_{13} = \sqrt{Q_0}\left(A Q_0 + (Kf - N)\mathrm{Re} R_{\mathrm{m}} S_1^2\right). \end{array} \tag{47}$$

Discussion

Figures 2–7 illustrate the behavior of the resulting parameters, i.e., the nanoparticle volume fraction ϕ, magnetic Reynolds number R_{m}, Strommer's number S_1, heat generation parameter Q_0, and heat flux parameter N for CNTs of various shapes in salt water. The effect of ϕ on the pressure gradient is illustrated in Fig. 2a. It is seen that an increase in the value of ϕ results in an increasing trend in the pressure gradient. It is also observed from this figure that the impact of ϕ on the pressure gradient is maximum for the zigzag shape but comparatively less for the chiral and minimum for the armchair shape. The effects of R_m and S_1 on the pressure gradient are shown in Fig. 2b, c, revealing that the pressure gradient is enhanced for higher values of R_m and S_1, for the CNTs of all three shapes (zigzag, chiral, and armchair). Meanwhile, Fig. 2d, e reveals that the pressure gradient decreases with an increase in the heat generation and heat flux parameter throughout the channel for the CNTs of different shapes.

Figure 3a–e shows the pumping characteristics in terms of the variation of the pressure rise per wavelength Δ_p with the time-averaged flux ($Q = F + 1$). Figure 3a shows the impact of the volume fraction ϕ on the pressure rise Δ_p, revealing that an increase of ϕ throughout the domain results in an increase in the pressure rise. Figure 3b illustrates that an increase in the value of R_m results in a higher pressure rise in the region $\left(\Delta_p < 0, Q < 0\right)$, but Δ_p goes down in the pumping region $\left(\Delta_p > 0, Q > 0\right)$. Figure 3c depicts the effect of S_1 on the pressure rise, revealing a similar behavior to that found for R_m. Figure 3d and e show the effects of Q_0 and N, respectively. Note that an increase in Q_0 and N results in a decrease in the pressure rise for the CNTs with zigzag, chiral, and armchair shapes in the entire domain.

Figure 4a–c shows the temperature distributions for different values of ϕ, Q_0, and N. Figure 4a shows that θ decreases when increasing ϕ for the CNTs of zigzag, chiral, and armchair shape. In Fig. 4b, c, a similar trend is noted for Q_0 and N. Note that θ increases when the values of Q_0 and N. are raised.

Figure 5 depicts the effects of the magnetic Reynolds and Strommer's numbers on h_x. Here, the induced magnetic field is in one direction in a half-region of the channel but the opposite direction in the other half-region. In addition, Fig. 5a illustrates that the magnitude of h_x decreases with increasing R_m from the wall h_1 to the middle of channel, whereas an increasing trend is seen in the other half of the channel. However, in Fig. 5b, the behavior of S_1 on h_x is opposite compared with that found for R_m.

Figure 6a, b shows the current density j_z for different values of R_m and S_1. In Fig. 6a, it is seen that, when increasing R_m, j_z increases, but j_z decreases when increasing S_1, as observed in Fig. 6b.

Figure 7a–e plots the velocity profile (u), showing an increase along the walls but a decrease in the middle of channel with increasing ϕ. Figure 7b, c illustrates R_m and S_1 for the CNTs with zigzag, chiral, and armchair shape, revealing conflicting behavior in the middle of the channel. Figure 7d shows the effect of the heat generation parameter Q_0 on the velocity profile u, revealing that the velocity increases with rising Q_0 in the middle of the channel, while the opposite behavior is seen at the channel walls.

Figure 7e demonstrates the effects of the Darcy number $\left(D_\alpha\right)$ on the velocity profile. It is seen that, near the walls, the velocity profile increases when increasing D_α, but at the center of the channel, a quite opposite behavior on the velocity profile is observed. The impact of α on the velocity profile is presented in Fig. 7f. Along the walls, the velocity profile decreases with increasing α, whereas at the center of the channel, a clear increase is observed.

To study the bolus phenomenon, streamlines of the Darcy number $\left(D_\alpha\right)$ for the CNTs with zigzag, chiral, and armchair shape are plotted in Figs. 8 to 10. It is found that the bolus is small for larger values of D_a.

In addition, the effects of significant physical parameters such as the nanoparticle volume fraction, heat generation, and heat flux on the skin friction coefficient and Nusselt number are computed numerically using MATLAB software and presented in Tables 2 to 7. Tables 2 and 3 are formulated for the nanoparticles of zigzag shape at the walls h_1 and h_2, respectively. Tables 4 and 5 present the results for the nanoparticles of chiral shape at the walls h_1 and h_2, respectively. Tables 6 and 7 are prepared for the nanoparticles with armchair shape at the walls h_1 and h_2, respectively. The results presented in these tables indicate that the absolute value of the skin friction coefficient is enhanced with increases in the volume fraction, heat generation parameter Q_0, and heat flux parameter N for the CNTs of all three shapes along both walls h_1 and h_2.

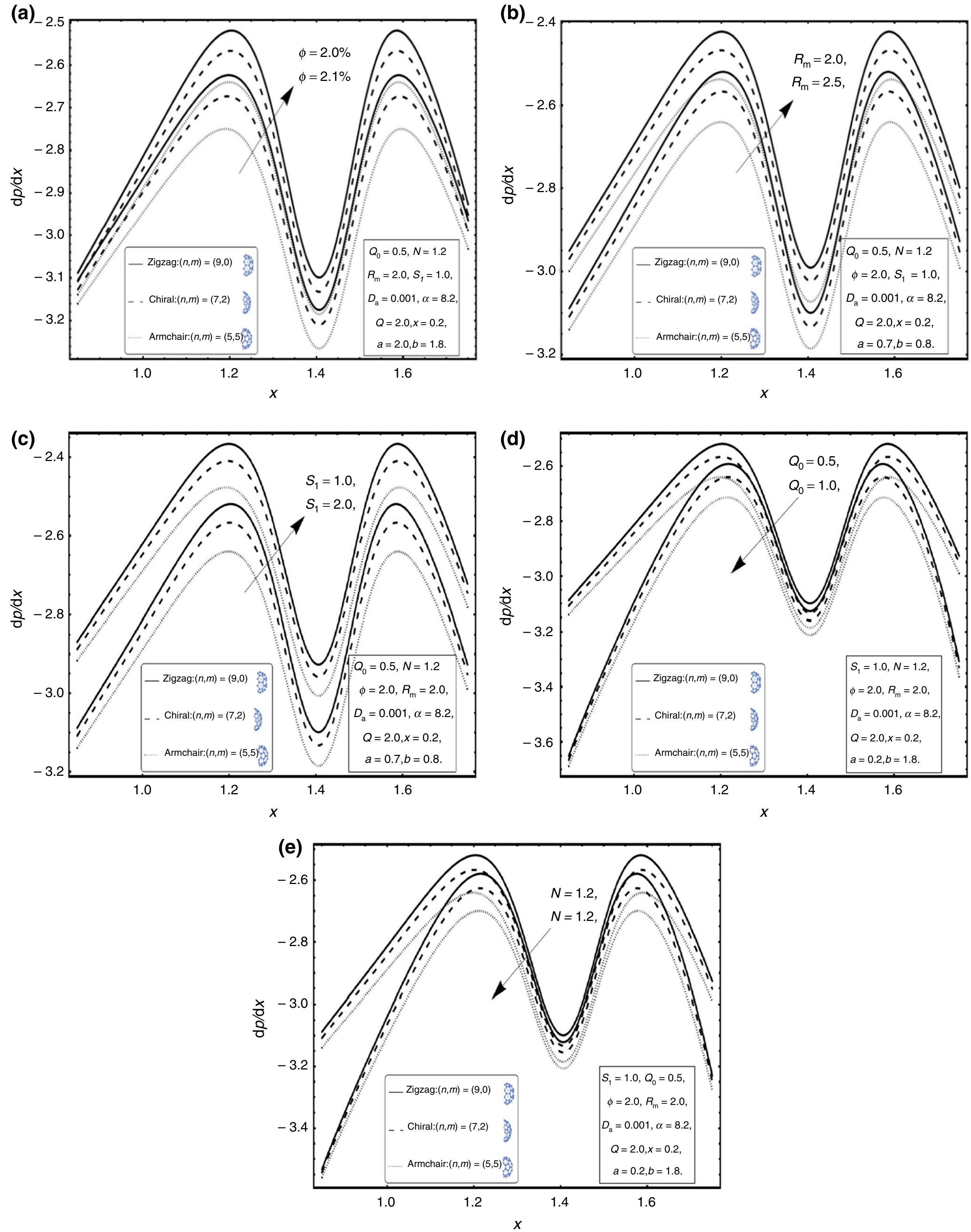

Fig. 2 **a–e** Variation of pressure gradient dp/dx for different flow parameters

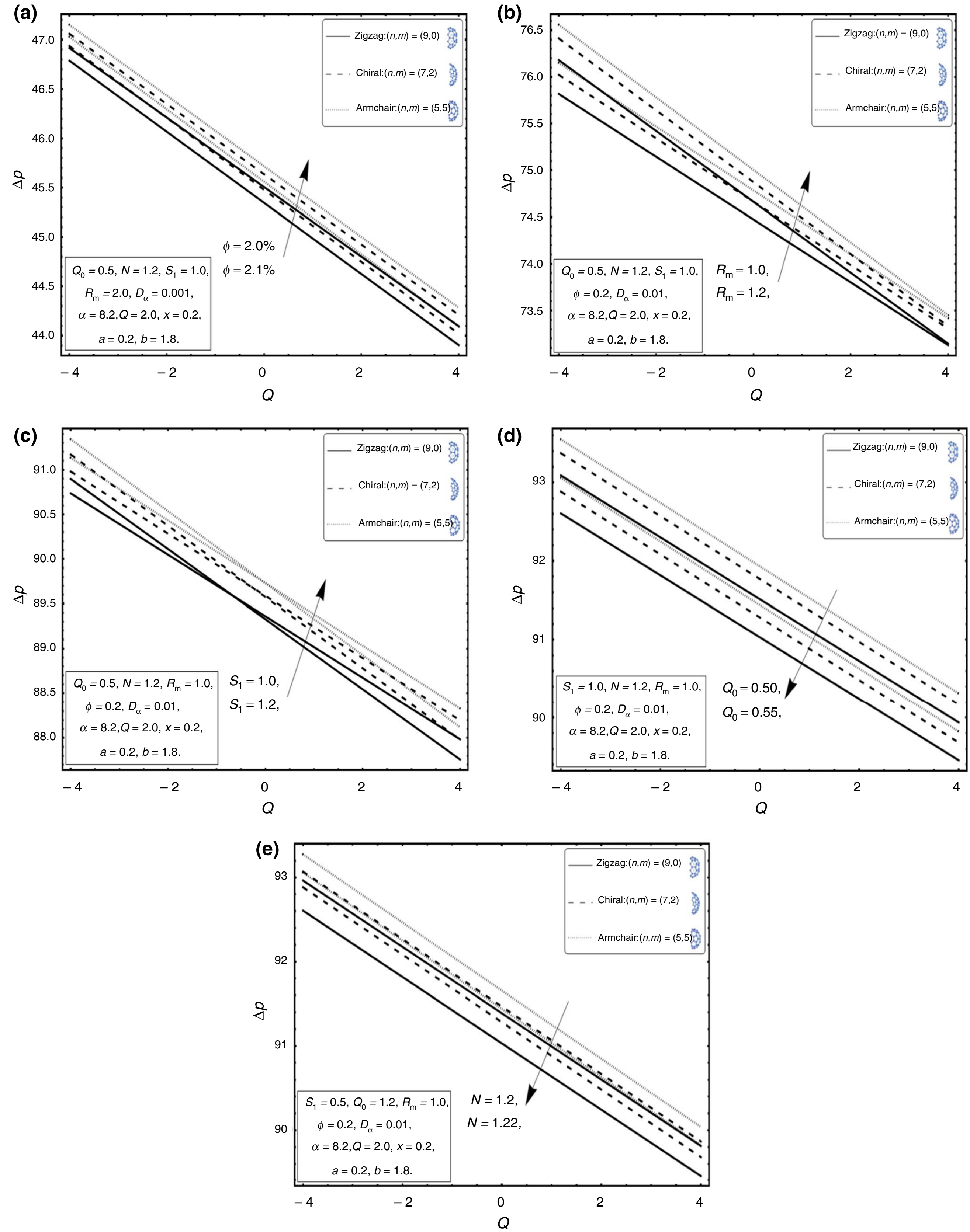

Fig. 3 **a**–**e** Variation of pressure rise Δp for different flow parameters

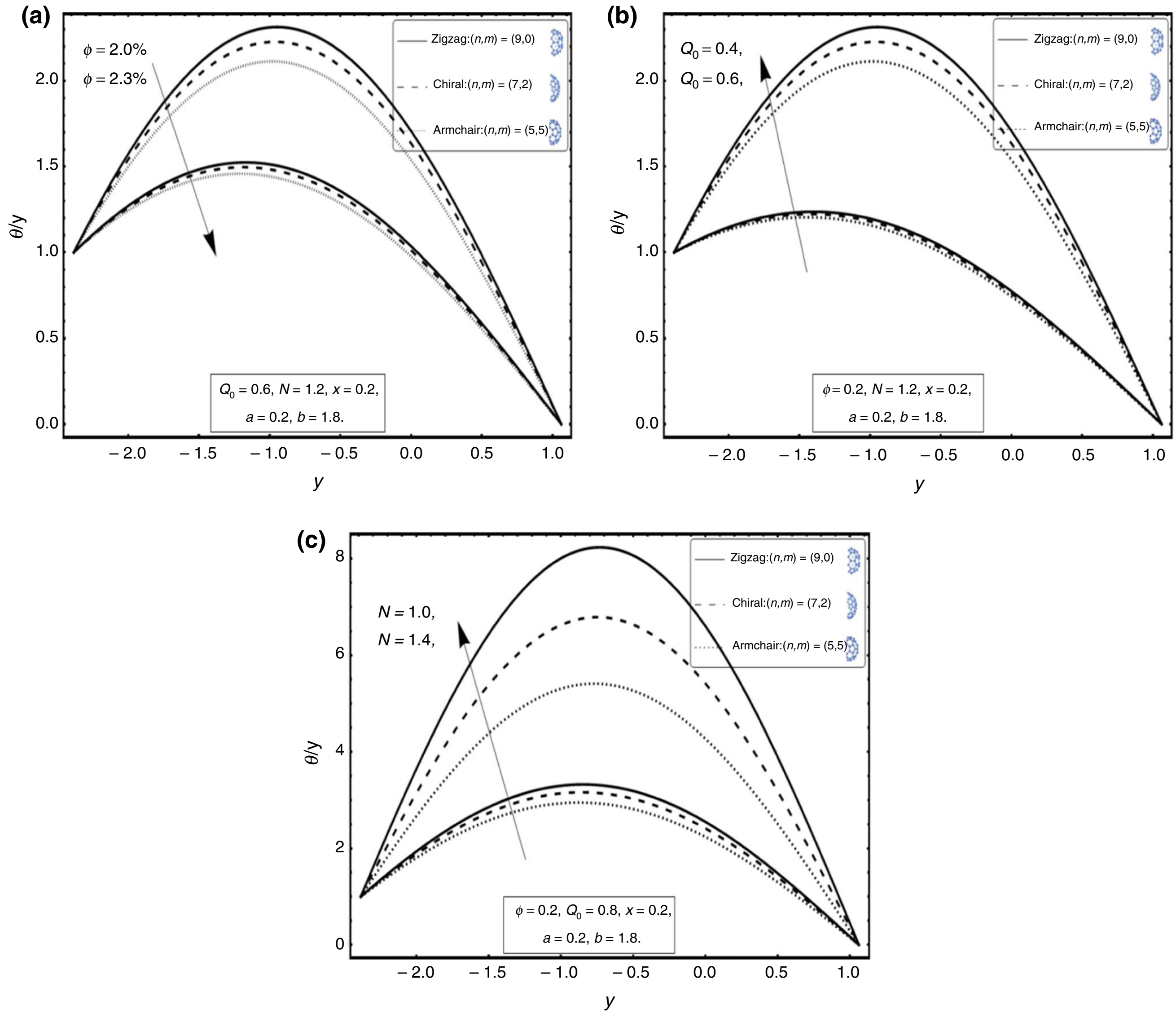

Fig. 4 **a–c** Variation of temperature profile θ for different flow parameters

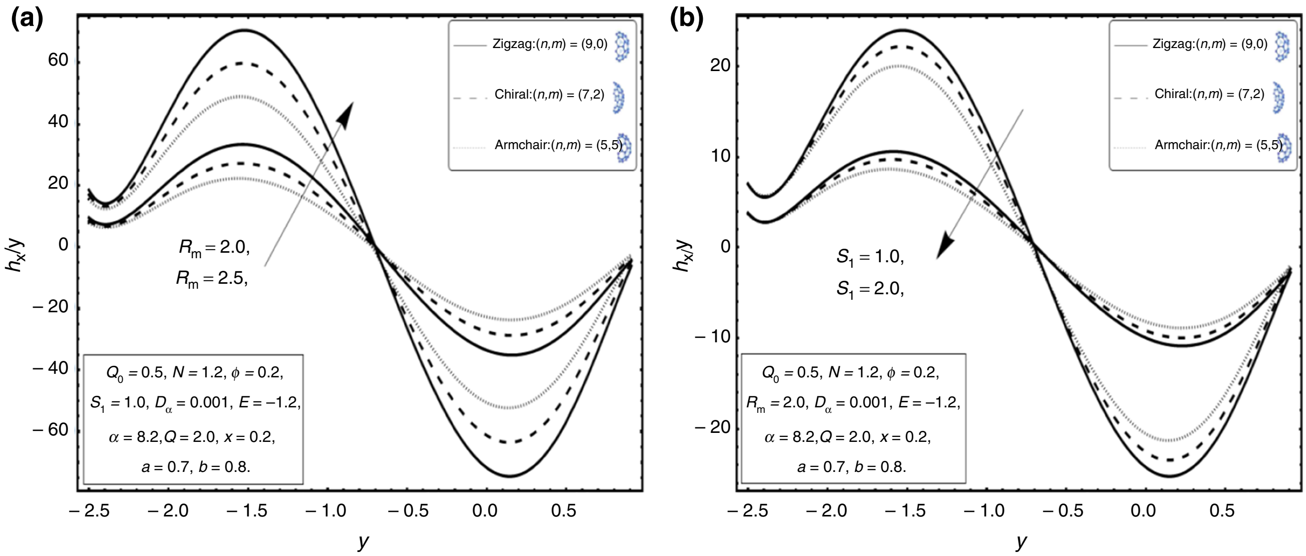

Fig. 5 **a**, **b** Variation of axially induced magnetic field h_x for different flow parameters

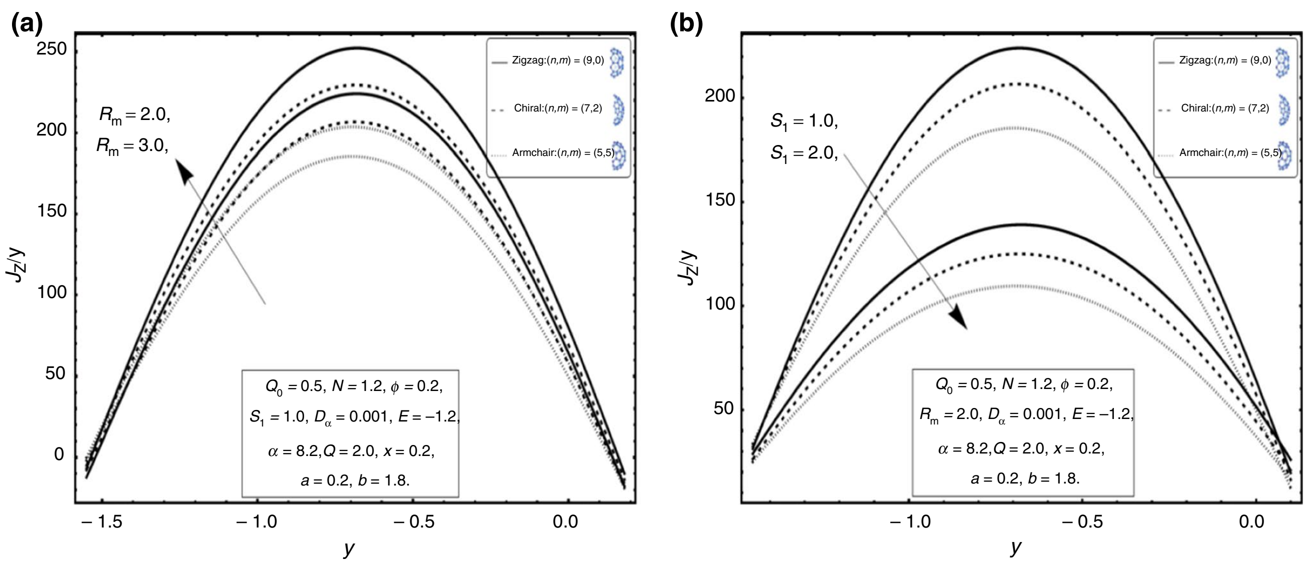

Fig. 6 **a**, **b** Variation of current density j_z for different flow parameters

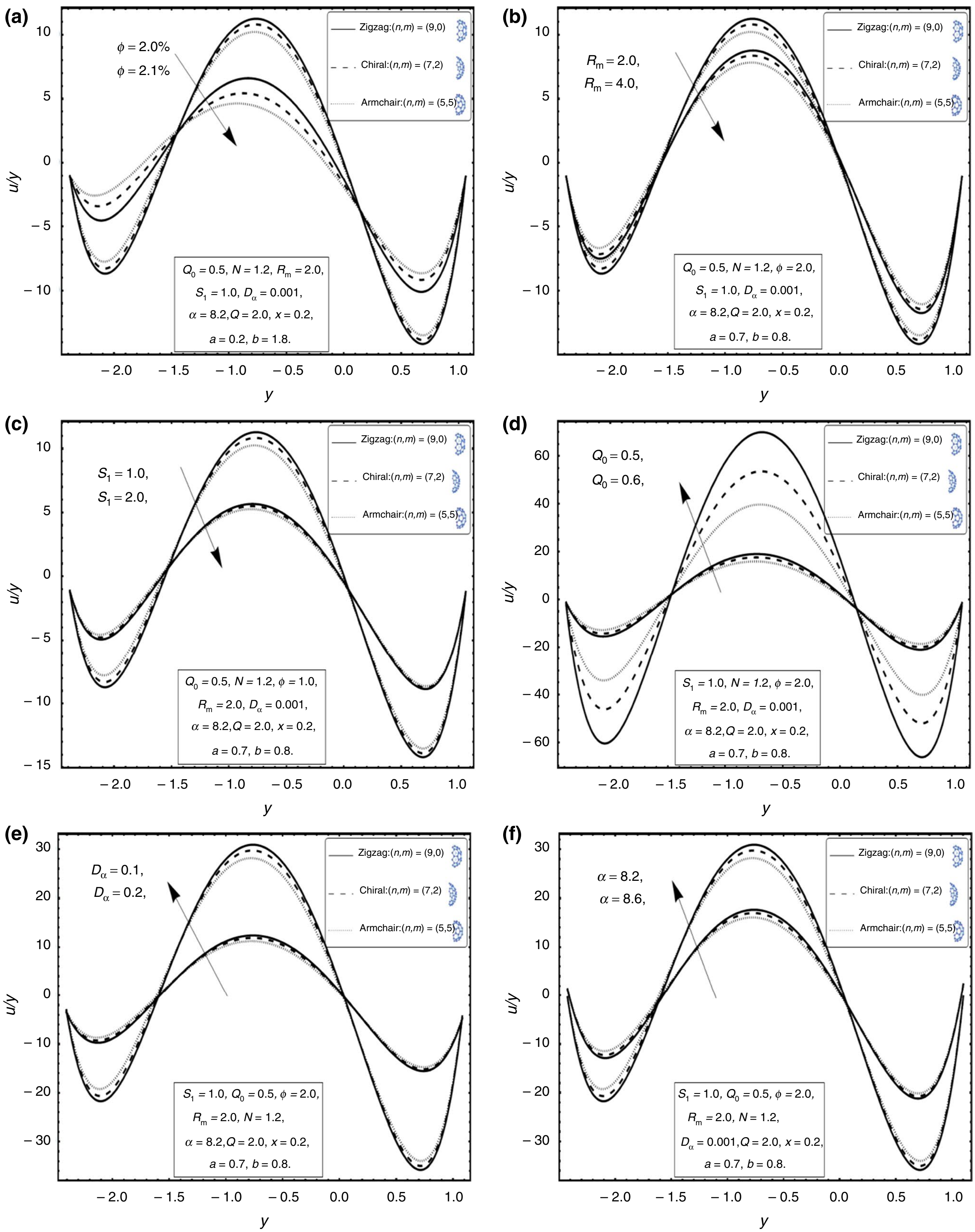

Fig. 7 **a**–**f** Variation of velocity profile u for different flow parameters

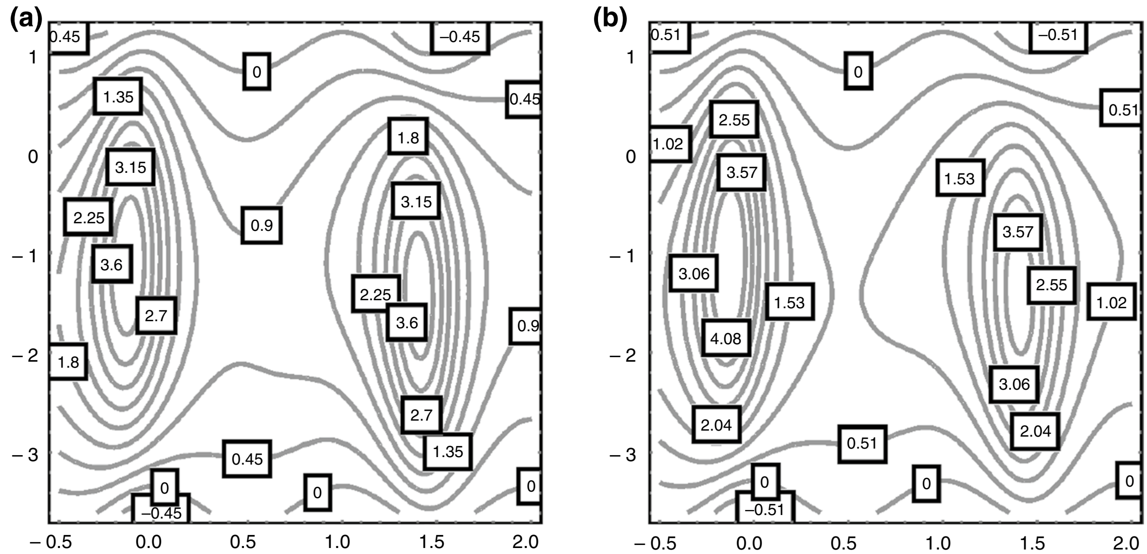

Fig. 8 **a**, **b** Streamlines for CNTs of zigzag shape for $D_\alpha = 0.1$ and $D_\alpha = 0.2$. The other parameters are $Q = 2.0,\ \alpha = 2.0,\ a = 0.7,\ b = 0.8,\ S_1 = 1.0,\ N = 0.02,\ D_\alpha = 0.002,\ Q_0 = 0.5$

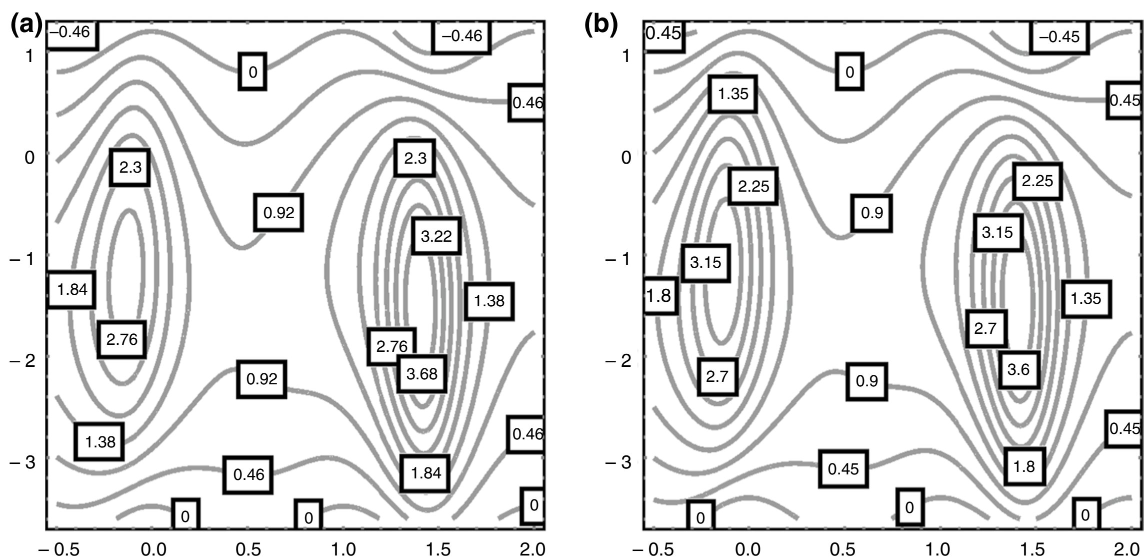

Fig. 9 **a**, **b** Streamlines for CNTs of chiral shape for $D_\alpha = 0.1$ and $D_\alpha = 0.2$. The other parameters are $Q = 2.0,\ \alpha = 2.0,\ a = 0.7,\ b = 0.8,\ S_1 = 1.0,\ N = 0.02,\ D_\alpha = 0.002,\ Q_0 = 0.5$

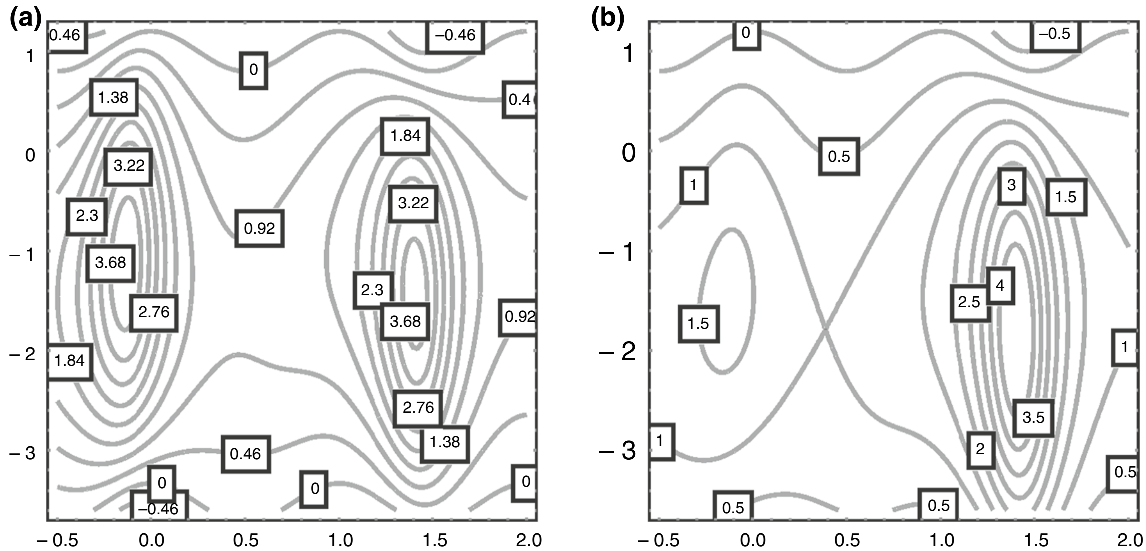

Fig. 10 **a**, **b** Streamlines for CNTs of armchair shape for $D_\alpha = 0.1$ and $D_\alpha = 0.2$. The other parameters are $Q = 2.0$, $\alpha = 2.0$, $a = 0.7$, $b = 0.8$, $S_1 = 1.0$, $N = 0.02$, $D_\alpha = 0.002$, $Q_0 = 0.5$

Table 2 Numerical values of skin friction coefficient and Nusselt number at wall h_1 when $x = 0.2$ for zigzag-shaped nanoparticles

ϕ	Q_0	N	C_f	Nu
0.02	0.6	1.2	−2.2621	−1.8093
0.03	0.6	1.2	−2.3035	−0.6252
0.04	0.6	1.2	−2.3496	−0.4522
0.025	0.4	1.0	−2.5712	−0.5112
0. 025	0.6	1.0	−2.6524	−0.7275
0. 025	0.8	1.0	−2.7248	−1.1282
0.035	0.7	1.1	−2.1754	−0.5573
0.035	0.7	1.3	−2.3121	−0.5974
0.035	0.7	1.5	−2.3857	−0.6514

Table 3 Numerical values of skin-friction coefficient and Nusselt number at wall h_2 when $x = 0.2$ for zigzag-shaped nanoparticles

ϕ	Q_0	N	C_f	Nu
0.02	0.6	1.2	2.5173	1.6317
0.03	0.6	1.2	2.5484	0.2480
0.04	0.6	1.2	2.5729	−0.0054
0.025	0.4	1.0	2.4887	0.0849
0.025	0.6	1.0	2.5449	0.3849
0.025	0.8	1.0	2.8412	0.8744
0.035	0.7	1.1	2.5531	0.1525
0.035	0.7	1.3	2.5756	0.2093
0.035	0.7	1.5	2.5841	0.2837

Table 4 Numerical values of skin friction coefficient and Nusselt number at wall h_1 when $x = 0.2$ for chiral-shaped nanoparticles

ϕ	Q_0	N	C_f	Nu
0.02	0.6	1.2	−2.2658	−1.6245
0.03	0.6	1.2	−2.3094	−0.6076
0.04	0.6	1.2	−2.3581	−0.4456
0.025	0.4	1.0	−2.5845	−0.5020
0.025	0.6	1.0	−2.6312	−0.7043
0.025	0.8	1.0	−2.7182	−1.0671
0.035	0.7	1.1	−2.1885	−0.5451
0.035	0.7	1.3	−2.3190	−0.5814
0.035	0.7	1.5	−2.4924	−0.6295

Table 5 Numerical values of skin friction coefficient and Nusselt number at wall h_2 when $x = 0.2$ for chiral-shaped nanoparticles

ϕ	Q_0	N	C_f	Nu
0.02	0.6	1.2	2.5214	1.4313
0.03	0.6	1.2	2.5546	0.2235
0.04	0.6	1.2	2.5810	0.0158
0.025	0.4	1.0	2.4837	0.0711
0.025	0.6	1.0	2.5198	0.3544
0.025	0.8	1.0	2.8291	0.8030
0.035	0.7	1.1	2.4722	0.1348
0.035	0.7	1.3	2.5835	0.1868
0.035	0.7	1.5	2.5920	0.2539

Table 6 Numerical values of skin friction coefficient and Nusselt number at wall h_1 when $x = 0.2$ for armchair-shaped nanoparticles

ϕ	Q_0	N	C_f	Nu
0.02	0.6	1.2	−2.2636	−1.7299
0.03	0.6	1.2	−2.3058	−0.6179
0.04	0.6	1.2	−2.3529	−0.4495
0.025	0.4	1.0	−2.5762	−0.5074
0.025	0.6	1.0	−2.6435	−0.718
0.025	0.8	1.0	−2.7225	−1.1027
0.035	0.7	1.1	−2.1863	−0.5523
0.035	0.7	1.3	−2.3147	−0.5908
0.035	0.7	1.5	−2.3883	−0.6423

Table 7 Numerical values of skin friction coefficient and Nusselt number at wall h_2 when $x = 0.21$ for armchair-shaped nanoparticles

ϕ	Q_0	N	C_f	Nu
0.02	0.6	1.2	2.5189	1.5459
0.03	0.6	1.2	2.5508	0.2379
0.04	0.6	1.2	2.5761	0.0096
0.025	0.4	1.0	2.4869	0.0793
0.025	0.6	1.0	2.5345	0.3724
0.025	0.8	1.0	2.8367	0.8447
0.035	0.7	1.1	2.5203	0.1452
0.035	0.7	1.3	2.5787	0.2001
0.035	0.7	1.5	2.5871	0.2714

Conclusions

The effects of addition of carbon nanotubes to a peristaltic flow in an induced magnetic field are studied, yielding the following key results:

- The effect of the nanoparticle volume fraction (ϕ) on the pressure gradient is least in the case of CNTs of armchair shape, being comparatively larger for chiral shape and maximum in case of zigzag shape.
- The pressure gradient decreases with an increase in the heat generation parameter.
- The pressure rise increases with an increase in the volume fraction or Reynolds and Strummer's number. It is also seen that increasing the heat flux parameter and Nusselt number decreases the pressure rise for the CNTs of zigzag, chiral, or armchair shape.
- The axial induced magnetic field decreases at the center of the right wall for higher values of the Strommer's number.
- The current density increases with increasing values of the magnetic Reynolds number, but declines with increasing Strommer's number.
- It is observed that the velocity profile increases with increase of the Darcy or Strommer's number at the middle of channel.
- The size of the bolus becomes small and the number of boluses reduces for higher values of the Reynold's number and Darcy number, for CNTs of zigzag, chiral, and armchair shape.
- The absolute value of the Nusselt number decreases when increasing ϕ but decreases when increasing Q_0 or N.

References

1. Latham TW. Fluid motion in a peristaltic pump MS thesis, Camb Mass Inst Technol. 1966.
2. Shapiro AH. Pumping and retrograde diffusion in peristaltic waves. In: Proceedings of workshop on ureteral reflux in children, Washington DC; 1967. p. 109–126.
3. Fung YC, Yih CS. Peristaltic transport. J Appl Mech. 1968;35:669–75.
4. Mishra M, Rao AR. Peristaltic transport of a Newtonian fluid in an asymmetric channel. Z Angew Math Phys (ZAMP). 2003;54:532–50.
5. Khan LA, Reza M, Mir NA, Ellahi R. Effects of different shapes of nanoparticles in peristaltic flow of MHD nanofluids filled in an asymmetric channel: a novel mode for heat transfer enhancement. J Therm Anal Calorim. 2019. https://doi.org/10.1007/s10973-019-08348-9.
6. Prakash J, Tripathi D, Triwari AK, Sait SM, Ellahi R. Peristaltic pumping of nanofluids through tapered channel in porous environment: applications in blood flow. Symmetry. 2019;11(7):868.
7. Riaz R, Ellahi R, Bhatti MM, Marin M. Study of heat and mass transfer in the Eyring-Powell model of fluid propagating peristaltically through a rectangular complaint channel. Heat Transf Res. 2019;50(16):1539–60.
8. Buongiorno J. Convective transport in nanofluids. J Heat Transf. 2006;128:240–50.
9. Choi S, Singer D, Wang H. Developments and applications of non-Newtonian flows. ASME Fed. 1995;66:99–105.
10. Masuda H, Ebata A, Teramae K, Hishinuma N. Alteration of thermal conductivity and viscosity of liquid by dispersing ultra-fine particles. Netsu Bussei. 1993;7(4):227–33.
11. Iijima S. Helical microtubules of graphitic carbon. Nature. 1991;354:56.
12. Baughman RH, Zakhidov AA, De Heer WA. Carbon nanotubes–the route toward applications. Science. 2002;297:787–92.
13. Zhan G-D, Kuntz JD, Wan J, Mukherjee AK. Single-wall carbon nanotubes as attractive toughening agents in alumina-based nanocomposites. Nat Mater. 2003;2:38.
14. Liu C, Huang H, Wu Y, Fan S. Thermal conductivity improvement of silicone elastomer with carbon nanotube loading. Appl Phys Lett. 2004;84:4248–50.
15. Sivakumar R, Guo S, Nishimura T, Kagawa Y. Thermal conductivity in multi-wall carbon nanotube/silica-based nanocomposites. Scr Mater. 2007;56:265–8.
16. Chu K, Wu Q, Jia C, Liang X, Nie J, Tian W, et al. Fabrication and effective thermal conductivity of multi-walled carbon nanotubes

reinforced Cu matrix composites for heat sink applications. Compos Sci Technol. 2010;70:298–304.
17. Raei B, Shahraki F, Jamialahmadi M, Peyghambarzadeh SM. Experimental study on the heat transfer and flow properties of γ-Al_2O_3/water nanofluid in a double-tube heat exchanger. J Therm Anal Calorim. 2017;127(3):2561–75.
18. Chen L, Xie H, Li Y, Yu W. Nanofluids containing carbon nanotubes treated by mechanochemical reaction. Thermochim Acta. 2008;477:21–4.
19. Saqib M, Ali F, Khan I, Sheikh NA, Shafie SB. Convection in ethylene glycol-based molybdenum disulfide nanofluid. J Therm Anal Calorim. 2019;135(1):523–32.
20. Rashidi S, Akbarzadeh M, Karimi N, Masoodi R. Combined effects of nanofluid and transverse twisted-baffles on the flow structures heat transfer and irreversibilities inside a square duct—a numerical study. Appl Therm Eng. 2018;130:135–48.
21. Asadollahi A, Rashidi S, Esfahani JA. Condensation process and phase-change in the presence of obstacles inside a minichannel. Meccanica. 2017;52:2265–74.
22. Duursma G, Sefiane K, Dehaene A, Harmand S, Wang Y. Flow and heat transfer of single-and two-phase boiling of nanofluids in microchannels. Heat Transf Eng. 2015;36:1252–65.
23. Majka TM, Raftopoulos KN, Pielichowski K. The influence of POSS nanoparticles on selected thermal properties of polyurethane-based hybrids. J Therm Anal Calorim. 2018;133(1):289–301.
24. Asadollahi A, Rashidi S, Mohamad AA. Removal of the liquid from a micro-object and controlling the surface wettability by using a rotating shell-Numerical simulation by lattice-Boltzmann method. J Mol Liq. 2018;272:645–55.
25. Mahian O, Kolsi L, Amani M, Estellé P, Ahmadi G, Kleinstreuer C, Marshall JS, Taylor RA, AbuNada E, Rashidi S, Niazmand H, Wongwises S, Hayat T, Kasaeian AB, Pop I. Recent advances in modeling and simulation of nanofluid flows—part II: applications. Phys Rep. 2019;791:1–59.
26. Nasiri H, Jamalabadi MYA, Sadeghi R, Safaei MR, Nguyen TK, Shadloo MS. A smoothed particle hydrodynamics approach for numerical simulation of nanofluid flows. J Therm Anal Calorim. 2019;135(3):1733–41.
27. Huang D, Wu Z, Sunden B. Effects of hybrid nanofluid mixture in plate heat exchangers. Exp Thermal Fluid Sci. 2016;72:190–6.
28. Khan I, Khan WA. Effect of viscous dissipation on MHD water-Cu and EG-Cu nanofluids flowing through a porous medium. J Therm Anal Calorim. 2019;135(1):645–56.
29. Malvandi A, Safaei M, Kaffash M, Ganji D. MHD mixed convection in a vertical annulus filled with Al2O3–water nanofluid considering nanoparticle migration. J Magn Magn Mater. 2015;382:296–306.
30. Bhatti MM, Abbas T, Rashidi MM. Entropy generation as a practical tool of optimisation for non-Newtonian nanofluid flow through a permeable stretching surface using SLM. J Comput Des Eng. 2017;4(1):21–8.
31. Bhatti MM, Abbas T, Rashidi M. Numerical study of entropy generation with nonlinear thermal radiation on magnetohydrodynamics non-Newtonian nanofluid through a porous shrinking sheet. J Magn. 2016;21:468–75.
32. Alamri SZ, Khan AA, Azeez M, Ellahi R. Effects of mass transfer on MHD second grade fluid towards stretching cylinder: a novel perspective of Cattaneo–Christov heat flux model. Phys Lett A. 2019;383:276–81.
33. Ellahi R, Sait SM, Shehzad N, Mobin N. Numerical simulation and mathematical modeling of electro-osmotic Couette-Poiseuille flow of MHD power-law nanofluid with entropy generation. Symmetry. 2019;11:1038.
34. Sarafraz MM, Pourmehran O, Yang B, Arjomandi M, Ellahi R. Pool boiling heat transfer characteristics of iron oxide nanosuspension under constant magnetic field. Int J Therm Sci. 2020;147:106131.
35. Alamri SZ, Ellahi R, Shehzad N, Zeeshan A. Convective radiative plane Poiseuille flow of nanofluid through porous medium with slip: an application of Stefan blowing. J Mol Liq. 2019;273:292–304.
36. Sheikholeslami M, Ellahi R, Shafee A, Li Z. Numerical investigation for second law analysis of ferrofluid inside a porous semi annulus: an application of entropy generation and exergy loss. Int J Numer Meth Heat Fluid Flow. 2019;29(3):1079–102.
37. Mamourian M, Shirvan KM, Pop I. Sensitivity analysis for MHD effects and inclination angles on natural convection heat transfer and entropy generation of Al_2O_3-water nanofluid in square cavity by response surface methodology. Int Commun Heat Mass Transf. 2016;79:46–57.
38. Shirvan KM, Mirzakhanlari S, Öztop HF, Mamourian M, Al-Salem K. MHD heat transfer and entropy generation in inclined trapezoidal cavity filled with nanofluid. Int J Numer Methods Heat Fluid Flow. 2017;27(10):2174–202.
39. Mekheimer KS. Peristaltic flow of a magneto-micropolar fluid: effect of induced magnetic field. J Appl Math. 2008;2008:570825.
40. Mekheimer KS. Effect of the induced magnetic field on peristaltic flow of a couple stress fluid. Phys Lett A. 2008;372:4271–8.
41. Nadeem S, Akbar NS. Influence of heat and mass transfer on the peristaltic flow of a Johnson Segalman fluid in a vertical asymmetric channel with induced MHD. J Taiwan Inst Chem Eng. 2011;42:58–66.
42. Jang SP, Choi SU. Role of Brownian motion in the enhanced thermal conductivity of nanofluids. Appl Phys Lett. 2004;84:4316–8.
43. Yu W, Choi S. The role of interfacial layers in the enhanced thermal conductivity of nanofluids: a renovated Hamilton-Crosser model. J Nanopart Res. 2004;6:355–61.